

## ARTICLE OPEN



## High-throughput deformation potential and electrical transport calculations

Ye Qing Jin<sup>1</sup>, Xiangdong Wang<sup>1,2</sup>, Mingjia Yao<sup>1</sup>, Di Qiu<sup>1,3</sup>, David J. Singh<sup>4</sup>, Jinyang Xi<sup>1,3</sup>, Jiong Yang<sup>1,3</sup>✉ and Lili Xi<sup>1,3</sup>✉

The deformation potential plays an important role in electrical transport properties, but in the context of high-throughput searches requires a consistent and readily computable reference level. Here, we design a high-throughput method for calculating the deformation potential for semiconductors in the MatHub-3d database. The deformation potential is obtained from the volume-dependent band edge (valence band maximum and conduction band minimum) variations with respect to the reference level. In order to adapt the calculation of reference level to a high-throughput manner, the average value of the first valence electron energy band associated with each compound is used as the reference level. Deformation potentials for 11,993 materials are calculated using the above-mentioned method. By considering the calculated deformation potentials, electronic structures, and bulk moduli, 9957 compounds with converged electrical transport properties are obtained. 332 promising p-type thermoelectric materials, and 321 n-type entries are then proposed. Among them, 156 compounds are screened to having both potentially good n- and p-type thermoelectric transport properties. The band structures and chemical bonding information for several typical compounds are further presented to reveal favorable band and bonding features for thermoelectrics.

*npj Computational Materials* (2023)9:190; <https://doi.org/10.1038/s41524-023-01153-x>

## INTRODUCTION

Thermoelectric (TE) materials are semiconductors that enable direct energy conversion between heat and electricity. They have wide application in space power, industrial waste heat recovery, local precise temperature control, and other fields<sup>1–5</sup>. The performance of TE materials is measured by the dimensionless figure of merit  $ZT$ , which is defined as  $ZT = (S^2\sigma T)/(\kappa_e + \kappa_L)$ , where  $S$  is the Seebeck coefficient,  $\sigma$  is the electrical conductivity,  $\kappa_e$  is the electronic thermal conductivity, and  $\kappa_L$  is the lattice thermal conductivity.  $S^2\sigma$  is the power factor (PF), which is an important parameter for characterizing the electrical transport properties. In general, desired TE performance requires high PF and low thermal conductivity. Due to complex and typically counter-correlated couplings of the different transport parameters<sup>6,7</sup>, the optimization of  $ZT$  and the development of new materials with high  $ZT$  have remained great challenges for decades.

High-throughput (HTP) computational screening has become an emerging tool to finding promising TE materials<sup>8–11</sup>. Ricci and Chen et al.<sup>12,13</sup> evaluated the electrical transport properties of 48,770 compounds with the constant relaxation time approximation (CRTA), based on the entries from the Materials Project<sup>14</sup>. Wang et al.<sup>15</sup> studied several thousands of compounds from AFLOW repository and analyzed the relationship between PFs and material structure parameters. Carrete et al.<sup>16</sup> combined constant-mean-free-path with the BoltzTraP code<sup>17</sup> to estimate the  $ZT$  of 75 nanograined half-Heusler compounds. Hong et al.<sup>18</sup> used data mining for the electronic structure of 3136  $X_2YZM_4$  quaternary compounds to identify electronic structure features that correlate with high  $S$  and low  $\kappa_L$ . Fan et al.<sup>19</sup> used first-principles calculates 127 chalcogenides and identified 46 compounds with maximum PF larger than

$10 \mu\text{Wcm}^{-1}\text{K}^{-2}$  out of 127 chalcogenides by HTP calculations. Yang et al.<sup>20</sup> predicted that NbFeSb is a potential p-type TE material by a HTP study. This prediction was subsequently conformed in an experimental study by Fu et al.<sup>21,22</sup>, who reported that FeNbSb is a p-type TE material, with a maximum  $ZT$  1.1 at 1100 K after Ti doping. Xi et al.<sup>23</sup> proposed a new type of high-performance TE material based on the deformation potential method, and some of the proposed entries were confirmed by experiments<sup>24</sup>.

Computation of the electrical transport properties within Boltzmann theory depends on two factors, the band structures and the charge carrier scatterings (i.e., the relaxation times). The electronic structures are generally available in databases and can be readily calculated within density functional theory; however, finding methods for obtaining relaxation times in a sufficiently accurate and HTP fashion is the key evaluation of electrical transport properties. The CRTA and/or the constant mean free path approximation have been widely used to predict electrical transport properties for HTP studies. However, the accuracy of the CRTA is often questioned as it neglects materials dependence for the relaxation time, while the constant mean free path method assumes an extreme nanostructured limit, neglecting materials dependence of the mean free path. Therefore, it is important to explore practical methods suited to HTP that go beyond these approximations. This requires a balance among robustness, efficiency, and accuracy.

In the case of TE materials, electron-phonon scattering is the most important mechanism, particularly at high temperature for materials doped to the levels needed for optimum TE performance. Furthermore, it is an intrinsic scattering mechanism that can be fully captured by ab initio calculations<sup>25</sup> as has

<sup>1</sup>Materials Genome Institute, Shanghai University, Shanghai 200444, China. <sup>2</sup>School of Physics and Electronic Science, East China Normal University, Shanghai 200241, China.

<sup>3</sup>Zhejiang Laboratory, Hangzhou, Zhejiang 311100, China. <sup>4</sup>Department of Physics and Astronomy, University of Missouri, Columbia, MO 65211, USA. ✉email: [jiongyang@tshu.edu.cn](mailto:jiongyang@tshu.edu.cn); [lilyxi@tshu.edu.cn](mailto:lilyxi@tshu.edu.cn)

been reported for half-Heusler<sup>26,27</sup>, Mg<sub>3</sub>Sb<sub>2</sub><sup>28,29</sup>, PbTe<sup>30,31</sup> and some other TE materials. However, while such calculations can provide accurate predictions of the electronic relaxation time, these methods are very time-consuming and not suitable for HTP calculations. An intermediate method is the deformation potential (DP) theory proposed in the 1950s, by Bardeen and Shockley<sup>32</sup>. This theory deals with electron-phonon scattering by longitudinal acoustic (LA) phonons. In this approximation, the electron-phonon coupling strength is simply equivalent to  $E_{DP}^2/C$ , where  $E_{DP}$  is the DP constant and  $C$  is Young's modulus<sup>33</sup>. Therefore, the deformation potential approximation (DPA) can predict the electron scattering time and further the electrical transport properties effectively. Xi et al.<sup>23</sup> evaluated the electronic transport of chalcogenides by the DPA and proposed Cd<sub>2</sub>Cu<sub>3</sub>In<sub>3</sub>Te<sub>8</sub> as a TE material. Jia et al.<sup>34</sup> used DP theory for 243 chalcogenides and identified 50 promising TE materials based on the results. Guo et al.<sup>35,36</sup> used DPA and single parabolic band model to compute the relaxation time and predict ZT of GeTe and SnSe. Hamdaoui et al.<sup>37</sup> predicted the carrier mobility of Cu<sub>2</sub>ZnGe<sub>4</sub> by DPA and proposed that Cu<sub>2</sub>ZnGeS<sub>4</sub> can be applied as a TE material. Yao et al.<sup>38</sup> screened the high mobility two-dimensional materials based on the DPA applied in HTP calculations. Thus, DP can be regarded as a reasonable approach that includes materials dependence, while maintaining practicality for HTP calculations. However, HTP methods work best when the underlying approaches are as unbiased as possible. This is an issue for DP calculations, because band structure methods use periodic boundary condition, and the absolute position of an energy level in an infinite periodic crystal is only defined to an unknown constant. As such, a reference level is thus required to obtain the band variations with respect to the volume changes that go into the DP constant,  $E_{DP}$ . Cardona and Christensen<sup>39</sup> assumed that the dielectric midgap energy level can be used as a constant reference. Wei and Zunger<sup>40</sup> have calculated the DPs by assuming that the energy level of deep core states are not sensitive to the volume deformation. Wei et al.<sup>41,42</sup> used the supercell uniaxial stretching method to calculate the DP. These methods are feasible for the calculation of individual systems, but they all have certain drawbacks in HTP calculation of DP. Here, we use the average value of the first valence electron energy band as the reference level. This is more amenable to HTP calculations than the use of deep core levels. This method is robust and efficient in HTP workflows, and we find that the accuracy is also acceptable comparing with solutions obtained in reported non-HTP studies (see below). We used this approach to obtain DPs and electrical transport properties for approximately 10,000 semiconducting entries in the MatHub-3d database<sup>43</sup>. Hundreds of new TE compounds are thus proposed. This provides transport data and demonstrates more accurate HTP evaluation of electrical properties than has been available in such large sets of data.

## RESULTS AND DISCUSSION

The data in this work are derived from the MatHub-3d database website<sup>43,44</sup>. 33,213 structural data with band structures are selected for further calculation. Since good TE materials are generally semiconductors, we first screen for systems with a band gap ( $E_g$ ) greater than 0.1 eV. This initial screen yields 11,993 candidates. A complete sequence of magnetic test, structural optimization, electron self-consistency, and energy band calculations was performed on these systems.

DPs can be obtained by the current HTP method, as shown in Fig. 1. The volume is changed to 98% $V_0$ , 99% $V_0$ ,  $V_0$ , 101% $V_0$ , 102% $V_0$  ( $V_0$  is the equilibrium volume), respectively, relative to the equilibrium structure by altering the scaling coefficients of the lattice vector. Then the electronic self-consistent calculations are

carried out for the five structures corresponding to the different volumes. The  $\mathbf{k}$ -grid used in the calculation of the self-consistent calculation is  $60/a + 1, 60/b + 1, 60/c + 1$ , where  $a, b$ , and  $c$  are the lattice constants of the systems. The DP can be obtained according to the following formula<sup>33,45</sup>:

$$E_{DP} = \frac{d(E - E_{ref})}{d(\ln V)}, \quad (1)$$

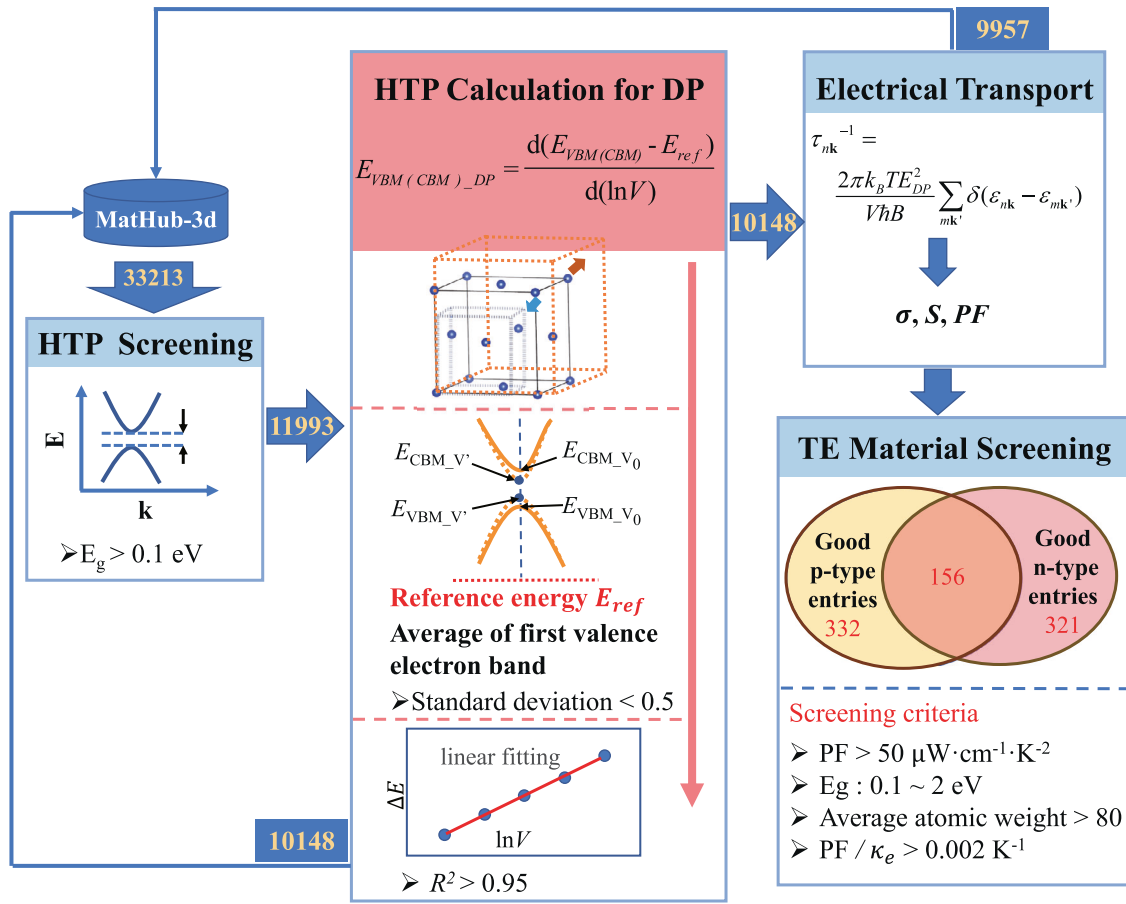
where  $V$  is the volume after extension and compression,  $E$  is the corresponding energy value of the valence band maximum (VBM) or conduction band minimum (CBM) and  $E_{ref}$  is the reference level, which is set as the average value of first valence electron energy band. Different choices made in non-HTP studies are contrasted with this reference level method in Supplementary Fig. 1. If the reference level is not set and instead the bare eigenvalues from the electronic structure code are used the results are very approximate, in the sense of disagreement with other approaches. The other two methods mentioned and DP calculated as in this work are distributed near the diagonal. This shows the feasibility of this method.

The linear fitting parameter  $R^2 > 0.95$  and standard deviation of reference energy level  $< 0.5$  eV are used as the screening standards for the removal of systems with the poor linear fitting of the DP. The results of different fitting  $R^2$  are shown in Supplementary Fig. 2. 10,148 compounds remain after this screening. These include 7,302 non-magnetic systems and 2,846 magnetic systems. The obtained DP data are displayed in the basic properties of MatHub-3d database website<sup>43</sup>. In addition, a summary table can be downloaded at MatHub-3d (<http://www.mathub3d.net/materials/about/DP.xlsx>).

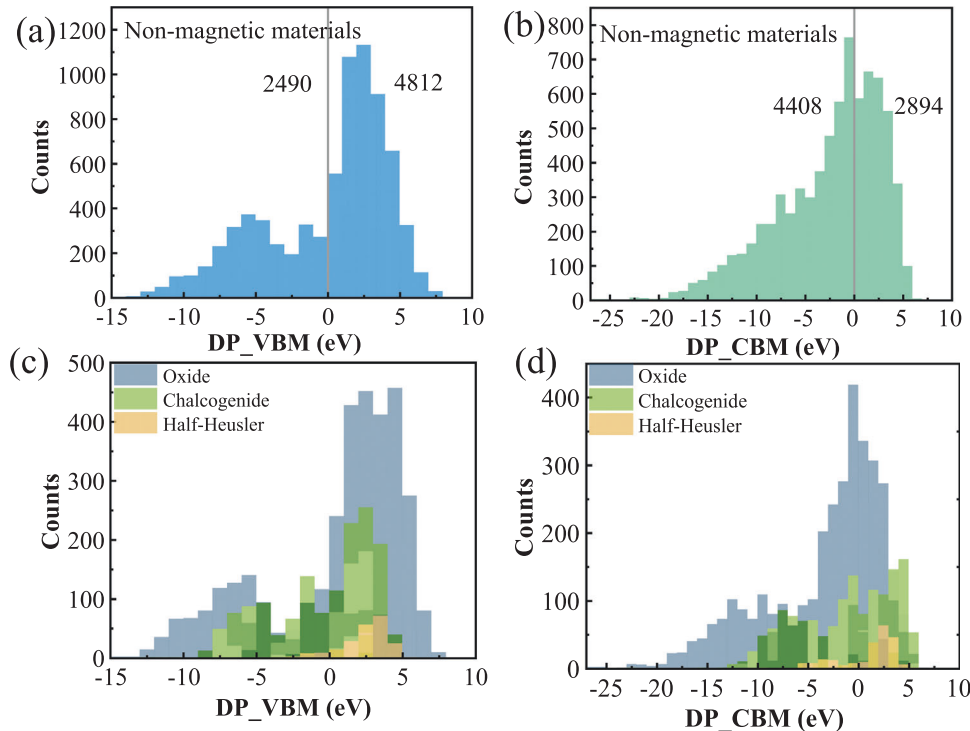
Figure 2a, b show distributions of DPs of nonmagnetic materials at VBM and CBM. As seen, the overall distribution of DPs is not symmetric around zero. From zero to the right, the distribution of positive DPs is very steep with values extending up to 8 eV in both (a) (b) figures. In contrast, the distribution of negative DPs decreases gradually from zero. But the negative DPs do not have a smooth gradient descent, especially for the VBM graph. These negative values extend up to -15 eV for the VBM, -25 eV for CBM. The trends of the numerical distributions are very similar in magnetic materials (Supplementary Fig. 3). More interestingly, the majority of the DPs at the VBM are above zero, while the DPs for CBM shows the opposite behavior.

Figure 2c, d show the DP data with oxides, chalcogenides, and half-Heuslers, which are materials classes containing TE materials. Results show that the distribution trend for oxide is similar to the overall distribution trend (Fig. 2a, b). Compared with oxides, chalcogenides have a smaller numerical distribution in the range of -10 eV ~ 5 eV. Half-Heusler compounds have the smallest distribution range, from -5 eV to 5 eV. As discussed in more detail below, low absolute values of the DP correspond to weaker scattering, and thus larger relaxation time. Thus, low magnitudes of the DP are favorable for TE performance. This is consistent with the observation that chalcogenides and half-Heuslers include many more good TE materials than oxides.

If we compress the lattice, i.e.,  $V' - V_0 = \Delta V < 0$ , and  $E_{VBM(CBM)} - E_{ref}$  increases (decreases), then  $E_{DP\_VBM(CBM)}$  is negative (positive). From the statistical data in Fig. 2c, it can be seen that  $E_{DP\_VBM}$  is positive for most of typical thermoelectric materials (oxides, chalcogenides, and half-Heusler) at VBM. That is, the energy of the VBM decreases with volume compression. At CBM,  $E_{DP\_CBM}$  is negative for most oxides and chalcogenides, while it is positive for most half-Heusler compounds. For most materials, VBMs of the majority materials (Fig. 2a) show positive values, similar with the cases in thermoelectric compounds (Fig. 2c), and CBMs (Fig. 2b) show negative values. Thus the band gaps will decrease when the volume increases in



**Fig. 1 Workflow diagram.** The workflow of high-throughput calculation.



**Fig. 2 Histogram of deformation potentials (DPs).** a, b DPs of nonmagnetic materials at VBM and CBM, (c, d) DPs involving oxide, chalcogenide and half-Heusler at VBM and CBM.

most of the materials (Supplementary Fig. 4a), such it does with normal thermal expansion. This corresponds to the Varshni effect<sup>46</sup>. This different behavior of the DP for the VBM and CBM leads to the fact that the majority of the band-gap DP are negative (As seen from the data of Supplementary Fig. 4a). As mentioned above, due to the positive value of  $E_{DP\_CBM}$  for half-Heusler compounds, the absolute average band-gap DP (Supplementary Fig. 4b) is small, 1.2 eV, smaller than that of the general compounds in the database (Supplementary Fig. 4a 3.2 eV).

The positive and negative changes in DP are related to the formation of band gap of materials. When the energy levels of the occupied state and the empty state form the valence and conduction bands respectively, the energy position of VBM decreases with increasing volume and weakening interatomic interaction, resulting in a negative  $E_{DP\_VBM}$ . Meanwhile, the  $E_{DP\_CBM}$  is positive. On the other hand, the energy band gap can also be formed by the interaction of a series of partially occupied electronic states. With increasing lattice constant, the interaction weakens and the band gap decreases, resulting in a positive  $E_{DP\_VBM}$  and a negative  $E_{DP\_CBM}$ . According to our HTP calculations of the DP, the latter case (band gap decreases with increasing lattice constant) is more common than the former.

The DP data, as above, were used to obtain the electrical transport properties of 10,148 compounds, and converged data was obtained for 9957 entries. The calculated results for a prototype compound, MatHub3d-84609 TiCoSb, are shown in Supplementary Fig. 5, including the Seebeck coefficient, electrical conductivity, and PF at 700 K and different carrier concentrations. The experimental results for p-type TiCoSb show that the PF can reach  $16 \mu\text{Wcm}^{-1}\text{K}^{-2}$  at  $750 \text{ K}^{47}$ , consistent with the predicted results in Figure Supplementary Fig. 5. The original data of the 9957 compounds can be viewed on the electrical transport properties section of MatHub-3d<sup>44</sup>. A temperature of 700 K is selected because TE materials are usually used at high temperatures and because this is within the important temperature range for energy applications in waste heat recovery. According to the Ioffe's criterion<sup>48</sup>, the highest PF generally occurs when the Seebeck coefficient is about  $180 \mu\text{V/K}^{49,50}$ , so we uniformly select the electrical conductivity and PF corresponding to this Seebeck coefficient. A summary data table can be found at MatHub-3d ([http://www.mathub3d.net/materials/about/electric\\_data.xlsx](http://www.mathub3d.net/materials/about/electric_data.xlsx)).

Figure 3a shows the PF distribution of 9957 materials at 700 K, both n-type and p-type. The result shows that PFs of most systems are within  $50 \mu\text{Wcm}^{-1}\text{K}^{-2}$ , but some systems are exceptions. Figure 3b, c show the relationship between PFs and DPs for p-type and n-type, respectively with absolute DP less than 6 eV. It can be seen from the diagram that PF and the absolute DP have obvious negative correlation relationship. This is expectable since strong scattering is unfavorable for electrical conductivity as seen in Eq. (5). Importantly, this shows that the band features that lead to high  $S$  coefficient do not lead necessarily to high DP in contrast to the band structure part of the conductivity, which is counter-correlated with  $S$ . The smaller the DP, such as less than 2 eV, the greater the PF. Supplementary Figs. 6 and 7 show the same trend at 300 K.

In order to further screen for materials with excellent TE properties, we design a HTP screening process. The screening criteria are as follow: 1.  $\text{PF} > 50 \mu\text{Wcm}^{-1}\text{K}^{-2}$ ; 2.  $E_g$  between 0.1 eV  $\sim$  2 eV; 3. The average atomic weight  $> 80$ ; 4.  $\text{PF}/\kappa_e > 0.002 \text{ K}^{-1}$ . The optimum  $E_g$  for TE applications are around  $10 k_B T_{\text{op}}$ , where  $T_{\text{op}}$  is the operating temperature<sup>48</sup>. It should be emphasized that the  $E_g$  is chosen within the range of 0.1 eV  $\sim$  2 eV considering the uncertainties of the calculations as well as the fact that this rule for the optimum band gap is often violated in actual thermoelectric materials. In addition, since the average atomic mass is directly related to the thermal conductivity, we

use the average atomic weight larger than 80 as a condition for rapid screening of low sound velocity and potentially low thermal conductivity materials<sup>23</sup>. This is important because at the present time there is no way to accurately and sufficiently quickly determine  $\kappa_L$  in the context of HTP. Even if the lattice thermal conductivity is neglected, high  $\kappa_e$  material is unfavorable. Therefore, an additional screening condition  $\text{PF}/\kappa_e$  is added after the initial screening. Finally, 321 n-type TE materials and 332 p-type TE materials are identified. Among them, 156 TE materials that are favorable for both p-type and n-type are found. Figure 3e, f show  $\text{PF}/\kappa_e$  values of these identified materials. Analysis shows that these compounds have lower DP constants in the range of  $-4 \sim 4 \text{ eV}$ .

Supplementary Table 1 lists  $E_g$ , DP, electrical conductivity, Seebeck coefficient, PF, and  $\text{PF}/\kappa_e$  for the 156 materials. Among them, some are previously reported TE materials with desirable properties, including  $\text{Bi}_2\text{Te}_3$ <sup>51–53</sup>,  $\text{PbS}^{54}$ ,  $\text{CoNbSn}^{55}$ ,  $\text{HfRhSb}^{56}$ ,  $\text{GeTe}^{57}$ ,  $\text{SeSn}^{58}$ , etc., and others. To illustrate the results, we select two typical compounds (i.e.,  $\text{MoTe}_2$  and  $\text{KSbSn}$ ) among the 156 entries to analyze their electronic structures and bonding characters in relation to TE performance. Figure 4a shows the band structure of  $\text{MoTe}_2$ . This compound has evident multi-valley band edges<sup>59</sup>. At CBM there is a degeneracy of 6 between  $\text{K}$  point and  $\Gamma$  point, the other two nearest valleys have a degeneracy of 4 at  $\text{K}$  point,  $\text{H}$  point has a degeneracy of 2, so that the effective total degeneracy of the conduction band edge is up to 12 depending on temperature and doping level. There are three energy valleys at VBM. The degeneracy at  $\text{K}$  point is 4 and the degeneracy at  $\text{H}$  point is 2. Combined with  $\Gamma$  points, the total degeneracy is 7. Owing to this multi-valley band feature,  $\text{MoTe}_2$  has a good electrical transport performance. The n-type PF is up to  $156 \mu\text{Wcm}^{-1}\text{K}^{-2}$  and p-type PF is  $80 \mu\text{Wcm}^{-1}\text{K}^{-2}$ .

For  $\text{KSbSn}$ , both the high p-type and n-type PFs can be attributed to the low DPs, around 0.5 eV at both VBM and CBM. The low DPs of this compound can be understood by the density of energy (DOE) and its integration  $E_{\text{band}}$  (divided by the equilibrium volume) (Fig. 4d). The  $E_{\text{band}}$  values are integrated within the energy range from  $E_{\text{VBM}}$  to  $E_{\text{VBM}} - 0.5 \text{ eV}$  and from  $E_{\text{CBM}}$  to  $E_{\text{CBM}} + 0.5 \text{ eV}$ .  $E_{\text{band}}$  is energetically resolved by the entire band energy and measures the destabilizing or stabilizing energy contributions of the chemical bonding. Small DP may then be attributed to the small bonding energy contribution near the band edge. The near-non-bonding state makes the corresponding band-edge bonding immune to volume change, resulting in a low DP. Compared with those of more than 7000 non-magnetic systems in Supplementary Fig. 8,  $\text{KSbSn}$  has a very small  $E_{\text{band}}$  and DP, which compensates the less favorable electronic structure of  $\text{KSbSn}$ , comparing to  $\text{MoTe}_2$ .

In this work, a practical HTP approach for DPs in the context of TE materials is proposed. The CBM and VBM DPs of 11,993 compounds are calculated and analyzed. While most of DPs at VBM are positive, most of DPs at CBM are negative, which is closely related to the bonding characters at VBM and CBM. Based on the DPA, the electrical transport properties of 9957 materials are evaluated. The statistics show that PF and the absolute DP have a clear negative correlation. In addition, we design an HTP screening process to screen out 332 p-type TE materials and 321 n-type TE materials with good performance. 156 compounds have both p-type and n-type properties, which can be attributed to multi-valley band structures / small DPs. The screened systems may be potential TE material candidates, which are worthy of further study. This work provides thus materials with the potential for high TE performance based on HTP screening. As such, it is expected that this will facilitate experimental searches for high-performance TE materials and



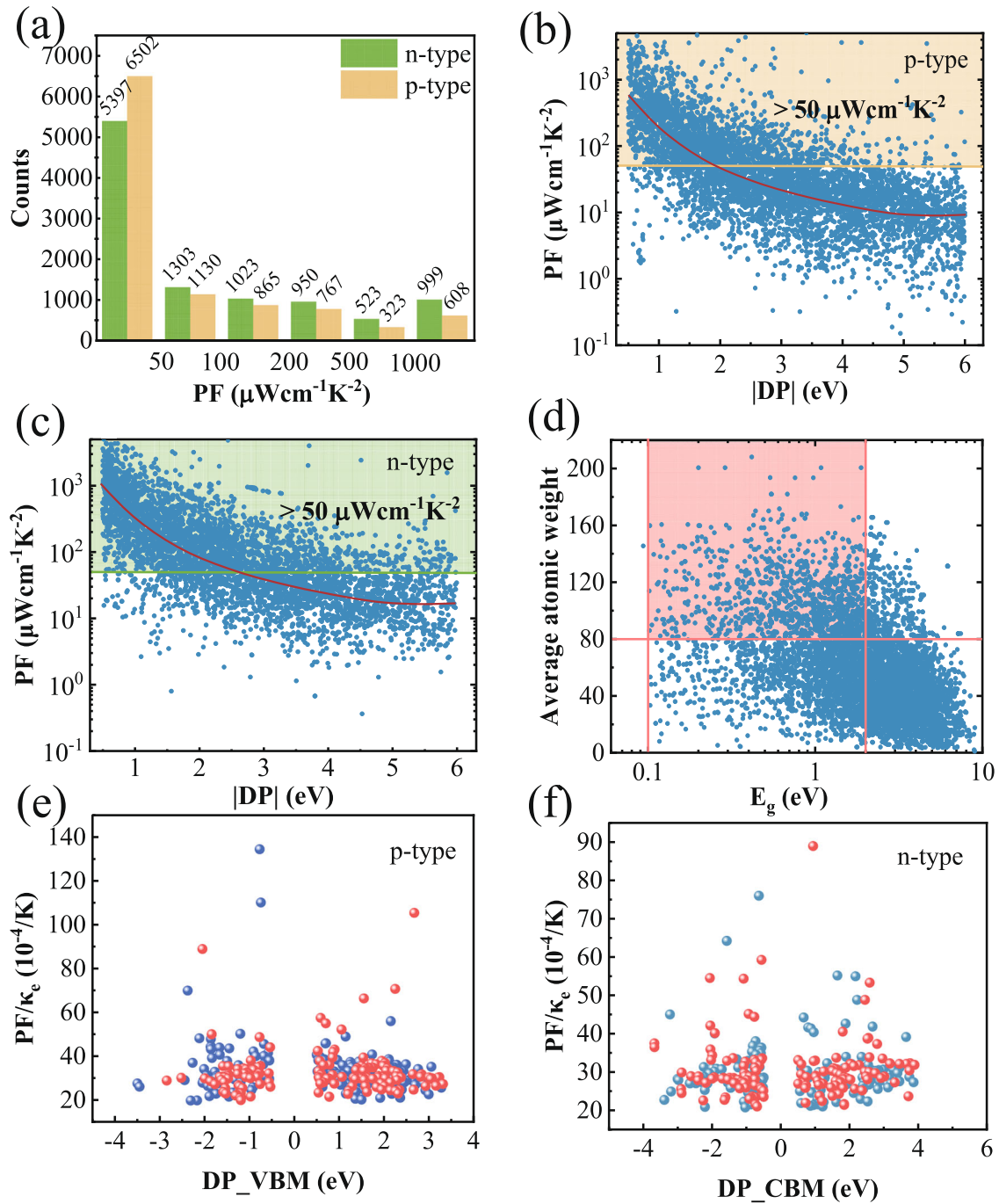


**Fig. 3** Transport properties of the calculated materials. **a** Distribution of PF under Seebeck coefficient  $180 \mu\text{V/K}$  at  $700 \text{ K}$ . **b, c** PF and absolute value of DP for n-type and p-type materials. **d**  $E_g$  and average atomic weights for all nonmagnetic materials. And colored boxes show filtered materials. **e, f** show  $\text{PF}/\kappa_e$  for p-type 332 compounds and n-type 321 compounds as to DP. Red balls represent that materials have good TE performance for both p- and n-type.

more rapid development of TE devices for energy and other technologies.

## METHODS

### Deformation potential and electrical transport properties calculation

All calculations are performed under the Vienna ab initio Simulation Package (VASP)<sup>60,61</sup> with the projector augmented

wave method<sup>62,63</sup> based on the density functional theory. The Perdew-Burke-Ernzerhof generalized gradient approximation is used as the exchange-correlation functional<sup>64</sup>. All the self-consistent calculations use  $520 \text{ eV}$  as the plane-wave energy cutoff energy and  $10^{-4} \text{ eV}$  as the energy convergence criterion. The pseudopotential files and Hubbard  $U$  values are the same as our previous study, where details may be found<sup>43</sup>.

In Boltzmann transport theory, the electrical conductivity  $\sigma$ , Seebeck coefficient  $S$  and electronic thermal conductivity  $\kappa_e$  can

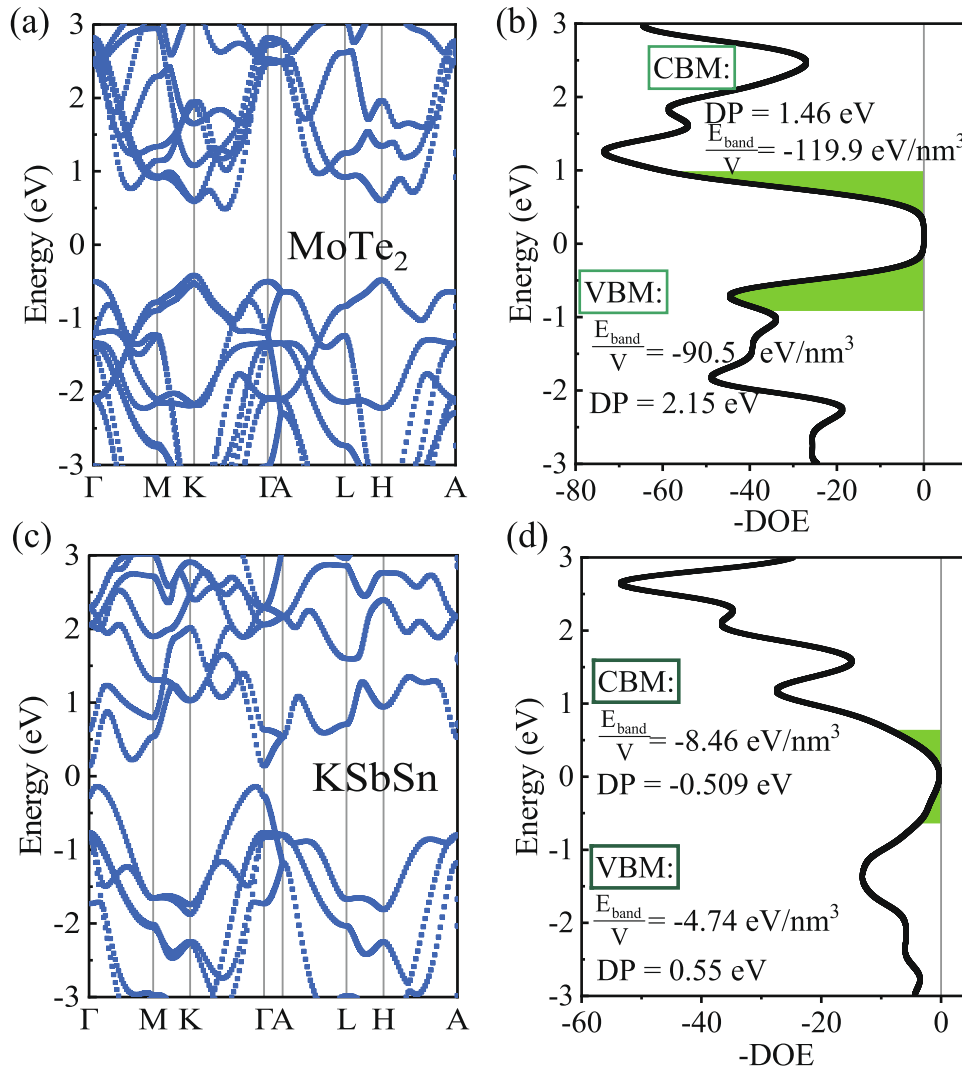


**Fig. 4** Band structures and DOE of the two TE compounds. **a** Band structures of MoTe<sub>2</sub>. **b** Density of energy (DOE) and integration  $E_{\text{band}}$  of MoTe<sub>2</sub>. **c** Band structures of KSbSn. **d** DOE and integration  $E_{\text{band}}$  of KSbSn.

be expressed as<sup>65</sup>:

$$\sigma_{\alpha\beta}(\mu, T) = \frac{1}{V} \sum_{\mathbf{n}\mathbf{k}} v_{n\mathbf{k}\alpha} v_{n\mathbf{k}\beta} \tau_{n\mathbf{k}} \left[ -\frac{\partial f_{\mu}(\varepsilon_{n\mathbf{k}}, T)}{\partial \varepsilon_{n\mathbf{k}}} \right], \quad (2)$$

$$S_{\alpha\beta}(\mu, T) = \frac{1}{eTV} \sigma_{\alpha\beta}(\mu, T)^{-1} \sum_{\mathbf{n}\mathbf{k}} v_{n\mathbf{k}\alpha} v_{n\mathbf{k}\beta} \tau_{n\mathbf{k}} (\mu - \varepsilon_{n\mathbf{k}}) \left[ -\frac{\partial f_{\mu}(\varepsilon_{n\mathbf{k}}, T)}{\partial \varepsilon_{n\mathbf{k}}} \right], \quad (3)$$

$$K_{\alpha\beta}(\mu, T) = \frac{1}{e^2 TV} \sum_{\mathbf{n}\mathbf{k}} v_{n\mathbf{k}\alpha} v_{n\mathbf{k}\beta} \tau_{n\mathbf{k}} (\mu - \varepsilon_{n\mathbf{k}})^2 \left[ -\frac{\partial f_{\mu}(\varepsilon_{n\mathbf{k}}, T)}{\partial \varepsilon_{n\mathbf{k}}} \right] - \frac{1}{eV} \sum_{\mathbf{n}\mathbf{k}} v_{n\mathbf{k}\alpha} v_{n\mathbf{k}\beta} \tau_{n\mathbf{k}} (\mu - \varepsilon_{n\mathbf{k}}) \left[ -\frac{\partial f_{\mu}(\varepsilon_{n\mathbf{k}}, T)}{\partial \varepsilon_{n\mathbf{k}}} \right] S_{\gamma\beta}(\mu, T), \quad (4)$$

Here,  $\varepsilon_{n\mathbf{k}}$  and  $\mathbf{v}_{n\mathbf{k}}$  are the electronic energy and group velocity, respectively, corresponding to band index  $n$  and reciprocal coordinate  $\mathbf{k}$ , and  $\tau_{n\mathbf{k}}$  is the electronic relaxation time.  $T$ ,  $\mu$ ,  $V$ ,  $f_{\mu}$  and  $e$  are, respectively, the absolute temperature, the Fermi level, the volume of the unit cell, the Fermi-Dirac distribution, and the electron charge.

The DP method is used to calculate electronic relaxation time. It is introduced to describe the scattering from long-wave LA phonons, and evaluated by calculating the two parameters of DP and Young modulus<sup>32</sup>. Considering the cost of HTP calculation,

here we use bulk modulus  $B$  instead of Young's modulus  $C$ . The bulk modulus is generated in the process of calculating the DP, and no additional calculation is required. The relaxation time is calculated using the following formula<sup>66</sup>:

$$\frac{1}{\tau_{n\mathbf{k}}} = \frac{2\pi k_B T E_{DP}^2}{V \hbar B} \sum_{m\mathbf{k}'} \delta(\varepsilon_{n\mathbf{k}} - \varepsilon_{m\mathbf{k}'}). \quad (5)$$

All of these parameters are implanted in software TransOpt 2.0<sup>67</sup>, which is suitable for electrical transport properties calculation by DPA.

The density of energy (DOE)<sup>68</sup> which can visualize the interaction of the anion and cation pairs in compounds sums up all off-site (interatomic) and on-site (atomic) contribution. It has advantages to the traditional COHP<sup>69,70</sup> (interatomic only) concept. DOE is implanted in LOBSTER program<sup>71</sup>. Negative (positive) -DOE represent antibonding (bonding) energy contributions. The energy integral of the -DOE is introduced to measure the weight of the bond energy contributions, which is written as:

$$E_{\text{band}} = \int_{E_{\text{VBM}}-0.5}^{E_{\text{VBM}}} -DOE(E) dE; E_{\text{band}} = \int_{E_{\text{CBM}}}^{E_{\text{CBM}}+0.5} -DOE(E) dE \quad (6)$$

where  $E_{\text{VBM}}$  and  $E_{\text{CBM}}$  are the energy at VBM and CBM, respectively. Fermi level is set as zero.

## DATA AVAILABILITY

The data that support the findings of this study are available from the corresponding author on reasonable request.

## CODE AVAILABILITY

Electrical transport properties calculation software TransOpt 2.0 can be available at <https://github.com/yangjio4849/TransOpt>.

Received: 9 May 2023; Accepted: 4 October 2023;

Published online: 14 October 2023

## REFERENCES

1. Goldsmid, H. J. Thermoelectric refrigeration, electrical engineering; Springer: Boston, MA, 2013.
2. Nolas, G. S., Sharp, J., & Goldsmid, H. J. Thermoelectrics: basic principles and new materials developments (Springer-Verlag, Heidelberg, 2001).
3. Bell, L. E. Cooling, heating, generating power, and recovering waste heat with thermoelectric systems. *Science* **321**, 1457–1461 (2008).
4. Poudel, B. et al. High-thermoelectric performance of nanostructured bismuth antimony telluride bulk alloys. *Science* **320**, 634–638 (2008).
5. LeBlanc, S. Thermoelectric generators: Linking material properties and systems engineering for waste heat recovery applications. *Sustain. Mater. Tech.* **1**, 26–35 (2014).
6. Nag, B. R. Electron transport in compound semiconductors (Springer Verlag, 1980).
7. Scheidemantel, T. J., Ambrosch-Draxl, C., Thonhauser, T., Badding, J. V. & Sofo, J. O. Transport coefficients from first-principles calculations. *Phys. Rev. B* **68**, 125210 (2003).
8. Ward, C. Materials genome initiative for global competitiveness. (2012).
9. Fan, T. & Oganov, A. R. Discovery of high performance thermoelectric chalcogenides through first-principles high-throughput screening. *J. Mater. Chem. C* **9**, 13226–13235 (2021).
10. Na, G. S. & Chang, H. A public database of thermoelectric materials and system identified material representation for data-driven discovery. *npj Comput. Mater.* **8**, 214 (2022).
11. Sierpeklis, O. & Cole, J. M. A thermoelectric materials database auto-generated from the scientific literature using ChemDataExtractor. *Sci. Data* **9**, 648 (2022).
12. Ricci, F. et al. Data Descriptor: An ab initio electronic transport database for inorganic materials. *Sci. Data* **4**, 170085 (2017).
13. Chen, W. et al. Understanding thermoelectric properties from high-throughput calculations: trends, insights, and comparisons with experiment. *J. Mater. Chem. C* **4**, 4414 (2016).
14. Jain, A. et al. Commentary: The Materials Project: A materials genome approach to accelerating materials innovation. *APL Mater.* **1**, 011002 (2003).
15. Wang, S. et al. Assessing the thermoelectric properties of sintered compounds via high-throughput ab-initio calculations. *Phys. Rev. X* **1**, 021012 (2011).
16. Carrete, J., Mingo, N., Wang, S. & Curtarolo, S. Nanograined half-Heusler semiconductors as advanced thermoelectrics: an ab-initio high-throughput statistical study. *Adv. Funct. Mater.* **24**, 7427–7432 (2014).
17. Madsen, G. K. H. & Singh, D. J. BoltzTraP. A code for calculating band-structure dependent quantities. *Comput. Phys. Commun.* **175**, 67–71 (2006).
18. Hong, A., Tang, Y. & Liu, J. High-throughput screening of quaternary compounds and new insights for excellent thermoelectric performance. *J. Phys. Chem. C* **125**, 24796–24804 (2021).
19. Fan, T. & Oganov, A. R. Discovery of high performance thermoelectric chalcogenides through first-principles high-throughput screening. *J. Mater. Chem. C* **38**, 13226–13235 (2021).
20. Yang, J. et al. Evaluation of Half-Heusler Compounds as Thermoelectric Materials: A theoretical Approach. *Adv. Funct. Mater.* **18**, 2880–2888 (2008).
21. Fu, C. G. et al. Band engineering of high performance p-type FeNbSb based half-Heusler thermoelectric materials for figure of merit  $zT > 1$ . *Energy Environ. Sci.* **1**, 216–220 (2015).
22. Fu, C. G. et al. Realizing high figure of merit in heavy-band p-type half-Heusler thermoelectric materials. *Nat. Commun.* **6**, 8144 (2015).
23. Xi, L. L. et al. Discovery of high-performance thermoelectric chalcogenides through reliable high-throughput material screening. *J. Am. Chem. Soc.* **140**, 10785–10793 (2018).
24. Pan, S. S. et al. Embedded in-situ nanodomains from chemical composition fluctuation in thermoelectric  $\text{A}_2\text{Cu}_3\text{In}_3\text{Te}_8$  (A = Zn, Cd). *Mater. Today Phys.* **17**, 100333 (2021).
25. Giustino, F. Electron-phonon interactions from first principles. *Rev. Mod. Phys.* **89**, 015003 (2017).
26. Zhou, J. et al. Large thermoelectric power factor from crystal symmetry-protected non-bonding orbital in half-Heuslers. *Nat. Commun.* **9**, 1721 (2018).
27. Samsonidze, G. & Kozinsky, B. Accelerated screening of thermoelectric materials by first-principles computations of electron-phonon scattering. *Adv. Energy Mater.* **8**, 1800246 (2018).
28. Huang, S., Wang, Z., Xiong, R., Yu, H. & Shi, J. Significant enhancement in thermoelectric performance of  $\text{Mg}_3\text{Sb}_2$  from bulk to two-dimensional monolayer. *Nano. Energy* **62**, 212–219 (2019).
29. Meng, F. et al. Anisotropic thermoelectric figure-of-merit in  $\text{Mg}_3\text{Sb}_2$ . *Mater. Today Phys.* **13**, 100217 (2020).
30. Song, Q., Liu, T., Zhou, J., Ding, Z. & Chen, G. Ab initio study of electron mean free paths and thermoelectric properties of lead telluride. *Mater. Today Phys.* **2**, 69–77 (2017).
31. He, J., Xia, Y., Naghavi, S., Ozolins, V. & Wolverton, C. Designing chemical analogs to PbTe with intrinsic high band degeneracy and low lattice thermal conductivity. *Nat. Commun.* **10**, 719 (2019).
32. Bardeen, J. & Shockley, W. Deformation potentials and mobilities in non-polar crystal. *Phys. Rev.* **80** (1950).
33. Xi, J. et al. Temperature-dependent structural fluctuation and its effect on the electronic structure and charge transport in hybrid perovskite  $\text{CH}_3\text{NH}_3\text{PbI}_3$ . *J. Comput. Chem.* **42**, 2213–2220 (2021).
34. Jia, T. et al. Screening promising thermoelectric materials in binary chalcogenides through high-throughput computations. *ACS Appl. Mater. Interfaces* **12**, 11852–11864 (2020).
35. Guo, D. et al. The n- and p-type thermoelectricity property of GeTe by first-principles study. *J. Alloy. Compd.* **810**, 151838 (2019).
36. Guo, D. et al. Enhanced out-of-plane thermoelectric performance of Cmcm SnSe phase by uniaxial strain. *Phys. Lett.* **384**, 126002 (2020).
37. Hamdaoui, J. E. et al. Ab Initio study of carrier mobility, thermodynamic and thermoelectric properties of kesterite  $\text{Cu}_2\text{ZnGeS}_4$ . *Int. J. Mol. Sci.* **23**, 12785 (2022).
38. Yao, M. et al. MatHub-2d: A database for transport in 2D materials and a demonstration of high-throughput computational screening for high-mobility 2D semiconducting materials. *Sci. China Mater.* **66**, 2768 (2023).
39. Cardona, M. & Christensen, N. E. Acoustic deformation potentials and heterostructure band offsets in semiconductors. *Phys. Rev. B* **35**, 6182 (1987).
40. Wei, S.-H. & Zunger, A. Predicted band-gap pressure coefficients of all diamond and zinc-blende semiconductors: Chemical trends. *Phys. Rev. B* **60**, 5404 (1999).
41. Li, Y. H. & Gong, X. G. Ab initio calculation of hydrostatic absolute deformation potential of semiconductors. *Appl. Phys. Lett.* **88**, 042104 (2006).
42. Li, Y. H. et al. Ab initio all-electron calculation of absolute volume deformation potentials of IV-IV, III-V, and II-VI semiconductors: The chemical trends. *Phys. Rev. B* **73**, 245206 (2006).
43. Yao, M. et al. Materials informatics platform with three dimensional structures, workflow and thermoelectric applications. *Sci. Data* **8**, 236 (2021).
44. <http://www.mathub3d.net/>.
45. Xi, J., Long, M., Tang, L., Wang, D. & Shuai, Z. First-principles prediction of charge mobility in carbon and organic nanomaterials. *Nanoscale* **4**, 4348–4369 (2012).
46. Varshni, Y. P. Temperature dependence of the energy gap in semiconductors. *Physica* **34**, 149–154 (1967).
47. Zhou, M., Feng, C., Chen, L. & Huang, X. Effects of partial substitution of Co by Ni on the high-temperature thermoelectric properties of TiCoSb-based half-Heusler compounds. *J. Alloy. Compd.* **391**, 194–197 (2005).
48. Ioffe, A. F. Thermoelements and thermoelectric cooling; Physics Today: London, UK (1956).
49. Guo, D. et al. The room-temperature thermoelectric property of PbTe enhanced by mean-free-path filtering. *J. Alloy. Compd.* **893**, 162296 (2022).
50. Mahan, G. D. Figure of merit for thermoelectrics. *J. Appl. Phys.* **65**, 1578–1583 (1989).
51. Yim, W. M. & Amith, A. Bi-Sb alloys for magneto-thermoelectric and thermomagnetic cooling. *Solid State Electron* **15**, 1141–1165 (1972).
52. Tokia, T. et al. Relationship between thermoelectric properties and formation of microstructure, and compressive strength and grain size of Bi-Te materials. *J. Ceram. Soc. Jpn.* **104**, 109–115 (1996).
53. Tang, C. et al.  $\text{Bi}_2\text{Te}_3$  single crystals with high room-temperature thermoelectric performance enhanced by manipulating point defects based on first-principles calculation. *RSC Adv.* **25**, 14422–14431 (2019).
54. Qing, Y. X. et al. Thermoelectric transport properties of PbS and its contrasting electronic band structures. *Scr. Mater.* **185**, 76–81 (2020).
55. Zeshan, M. et al. Ab initio design of new cobalt-based half-Heusler materials for thermoelectric applications. *Phys. Rev. Mater.* **1**, 075407 (2017).

56. Kaur, K., Kumar, R. & Rai, D. P. A promising thermoelectric response of HfRhSb half Heusler compound at high temperature: A first principle study. *J. Alloy. Compd.* **763**, 1018–1023 (2018).
57. Li, J. et al. Electronic origin of the high thermoelectric performance of GeTe among the p-type group IV monotellurides. *NPG Asia Mater.* **9**, e353 (2017).
58. Zhao, L. et al. Ultralow thermal conductivity and high thermoelectric figure of merit in SnSe crystals. *Nature* **508**, 373–377 (2014).
59. Pei, Y. et al. Convergence of electronic bands for high performance bulk thermoelectrics. *Nature* **473**, 66–69 (2011).
60. Kresse, G. & Hafne, J. Ab initio molecular dynamics for liquid metals. *Phys. Rev. B* **47**, 558–561 (1993).
61. Kresse, G. & Furthmüller, J. Efficient iterative schemes for ab initio total-energy calculations using a plane-wave basis set. *Phys. Rev. B* **54**, 11169–11186 (1996).
62. Kresse, G. & Joubert, D. From ultrasoft pseudopotentials to the projector augmented-wave method. *Phys. Rev. B* **59**, 1758–1775 (1999).
63. Blöchl, P. E. Projector augmented-wave method. *Phys. Rev. B* **50**, 17953–17979 (1994).
64. Perdew, J. P., Burke, K. & Ernzerhof, M. Generalized gradient approximation made simple. *Phys. Rev. Lett.* **77**, 3865–3868 (1996).
65. Yang, J. et al. Electrical transport properties of filled CoSb<sub>3</sub> skutterudites: A Theoretical Study. *J. Electron. Mater.* **38**, 1397–1401 (2009).
66. Li, X. et al. TransOpt: A code to solve electrical transport properties of semiconductors in constant electron-phonon coupling approximation. *Comput. Mater. Sci.* **186**, 110074 (2021).
67. Zhang, J. et al. Intrinsic defects and the influences on electrical transport properties in quaternary diamond-like compounds: Cd<sub>2</sub>Cu<sub>3</sub>In<sub>3</sub>Te<sub>8</sub> as an example. *J. Mater. Sci.* **8**, 1222 (2022).
68. Küpers, M. S. M. et al. Ge-Ge contacts in the two-dimensional Ge<sub>4</sub>Se<sub>3</sub> Te phase and analysis of their chemical cause with the density of energy (DOE) function. *Angew. Chem. Int. Ed.* **56**, 10204–10208 (2017).
69. Deringer, V. L., Tchougreeff, A. L. & Dronskowski, R. Crystal orbital hamilton population (COHP) analysis as projected from plane-wave basis sets. *J. Phys. Chem. A* **115**, 5461–5466 (2011).
70. Maintz, S., Deringer, V. L., Tchougreeff, A. L. & Dronskowski, R. Analytic projection from plane-wave and PAW wavefunctions and application to chemical-bonding analysis in solids. *J. Comput. Chem.* **34**, 2557–2567 (2013).
71. Maintz, S., Deringer, V. L., Tchougreeff, A. L. & Dronskowski, R. LOBSTER: A tool to extract chemical bonding from plane-wave based DFT. *J. Comput. Chem.* **37**, 1030–1035 (2016).

## ACKNOWLEDGEMENTS

This work was supported by the Natural Science Foundation of China (Grant Nos. 52172216 and 92163212), Key Research Project of Zhejiang Laboratory (No. 2021PE0AC02), the National Key Research and Development Program of China (No.

2021YFB3502200), Shanghai Engineering Research Center for Integrated Circuits and Advanced Display Materials, and Shanghai Technical Service Center of Science and Engineering Computing, Shanghai University.

## AUTHOR CONTRIBUTIONS

The initial idea was proposed by J.Y. and L.X. Y.J. performed the high-throughput calculations. All authors participated in dataset analysis, writing and reviewing manuscript. J.Y. managed the project.

## COMPETING INTERESTS

The authors declare no competing interests.

## ADDITIONAL INFORMATION

**Supplementary information** The online version contains supplementary material available at <https://doi.org/10.1038/s41524-023-01153-x>.

**Correspondence** and requests for materials should be addressed to Jiong Yang or Lili Xi.

**Reprints and permission information** is available at <http://www.nature.com/reprints>

**Publisher's note** Springer Nature remains neutral with regard to jurisdictional claims in published maps and institutional affiliations.



**Open Access** This article is licensed under a Creative Commons Attribution 4.0 International License, which permits use, sharing, adaptation, distribution and reproduction in any medium or format, as long as you give appropriate credit to the original author(s) and the source, provide a link to the Creative Commons license, and indicate if changes were made. The images or other third party material in this article are included in the article's Creative Commons license, unless indicated otherwise in a credit line to the material. If material is not included in the article's Creative Commons license and your intended use is not permitted by statutory regulation or exceeds the permitted use, you will need to obtain permission directly from the copyright holder. To view a copy of this license, visit <http://creativecommons.org/licenses/by/4.0/>.

© The Author(s) 2023